Attenuation Correction of ^{99m}Tc-MAA SPECT Images for ^{90}Y-labeled Glass Microspheres Liver Radioembolization

Extended Abstract of the Thesis to obtain the Master of Science Degree in Biomedical Engineering

Laura Demino

Instituto Superior Técnico, Lisboa, Portugal

October 2017

Abstract

Yttrium-90 (^{90}Y)-labeled glass microspheres liver radioembolization is an effective treatment for unresectable hepatic tumors, with increasing clinical attention. In order to maximize the therapeutic efficacy while reducing the radiation-induced side effects, its treatment planning is based on Technetium-99m (^{99m}Tc)-labeled Macro-Aggregated Albumin (MAA) Single Photon Emission Computed Tomography (SPECT) imaging. However, photons interaction with human tissues and, in particular, ^{99m}Tc γ-rays attenuation, significantly compromise the accuracy of radioactivity quantification in diagnostic nuclear medicine. The aim of this thesis is to evaluate the impact of a personalized liver radioembolization treatment planning, which relies on Computed Tomography (CT)-based attenuation corrected ^{99m}Tc-MAA SPECT images. In a preliminary part of the conducted study, phantom models were employed to validate the methodology developed. Afterwards, clinical ^{99m}Tc-MAA SPECT were retrospectively corrected for attenuation, and their influence in ^{90}Y liver radioembolization dosimetry was quantitatively assessed. The proposed approach proved to accurately enable quantitative SPECT studies. Moreover, attenuation corrected ^{99m}Tc-MAA SPECT images permitted to statistically improve the agreement between predictive and post-treatment dosimetry maps. However, pre-and-post treatment dose maps often exhibited poor correlation, which may have been caused by distinct *in vivo* relative biologic distribution of ^{90}Y microspheres and MAA fragments, discrepancies in catheter positioning during treatment planning and treatment itself, as well as by noisy post-treatment ^{90}Y Positron Emission Tomography (PET)-CT images. For these reasons, in the future, research should address, in greater depth, the issues related to the differences between pre-and-post treatment dose maps.

Keywords: Hepatic Tumors, ^{90}Y Liver Radioembolization, ^{99m}Tc-MAA SPECT Imaging, CT-based Attenuation Correction, Patient-Specific Radionuclide Dosimetry

1 Introduction

Primary and metastatic hepatic tumors are one of the most common forms of cancer worldwide, leading to more than 1 million of new people affected annually [1]. Liver tumor treatment has always been quite challenging due to the severity and frequently multifocal nature of this pathology. Surgical tumor resection and liver transplantation are often unfeasible due to the advanced stage of the disease, and may be considered as successful treatment options only for early-diagnosed tumors [1, 2]. In this regard, Yttryum-90 glass microspheres (^{90}Y- microS; TheraSphere®, MDS Nordion, Ottawa, Canada) liver radioembolization is emerging as a promising treatment strategy for unresectable hepatic tumors. As in brachytherapy, during liver tumor radioembolization, the radioactive source is localized within the tumor proximity. In particular, the intrahepatic arterial administration of ^{90}Y microspheres is believed to preferentially deliver the therapeutic dose to the tumor, sparing the healthy liver parenchyma [3]. Thus, the injected ^{90}Y microspheres embolize the tumor feeding distal arterioles and induce the death of the hypervascularized tumor areas through the spontaneous decay of ^{90}Y [4, 5]. In order to maximize the therapeutic response and reduce the radiation-induced side effects, an appropriate treatment planning is of primary importance. In this respect, nuclear medicine provides a unique contribution. Specifically, Technetium-99m (^{99m}Tc)-labeled Macro-Aggregated Albumine (MAA) Single Photon Emission Computed Tomography (SPECT) imaging permits to improve the dosimetry evaluation of liver radioembolization treatment by providing an estimation of the metabolically active tumor and, hence, of the therapeutic microspheres biologic distribution [2, 4, 6–8]. However, the quantitative accuracy of SPECT imaging depends on multiple factors, including the attenuation effects, which mostly contribute to image degradation and may significantly compromise the radioembolization treatment planning and its efficacy [9].

This thesis aims to assess the impact of patient-specific attenuation correction of ^{99m}Tc-MAA SPECT imaging in the context of liver radioembolization, based on separately acquired Computed Tomography (CT) images. In this regard, to validate the CT-based attenuation correction method developed, a preliminary study on phantom models was conducted. This was followed by a critical analysis of attenuation uncorrected and retrospectively corrected clinical ^{99m}Tc-MAA SPECT images. Further, the quantitative accuracy of the implemented methodology was verified, and a dosimetry study was performed in order to assess the agreement between personalized pre-and-post treatment dose maps, derived from uncorrected or attenuation corrected ^{99m}Tc-MAA SPECT and ^{90}Y Positron Emission Tomography (PET)-CT images, respectively.

2 Materials and Methods

2.1 Physical Phantoms and Clinical Data Acquisition

The acquisition of ^{99m}Tc SPECT phantom images, clinical pre-treatment ^{99m}Tc-MAA and CT images, and post-treatment ^{90}Y PET images, was performed at the Nuclear Medicine Department of Champalimaud Foundation, Center for the Unknown, Lisbon. ^{99m}Tc radioisotope-based SPECT imaging was performed using a BrightView SPECT system (PHILIPS, Amsterdam,The Netherlands), while CT and PET imaging through a PET-CT GEMINI TF system (PHILIPS, Amsterdam, The Netherlands).

Cylindrical phantom, with uniform activity distribution, and National Electrical Manufacturers Association (NEMA) IEC Body Phantom models were employed. In particular, the latter consists of a body phantom, presenting six spherical inserts of 10, 13, 17, 22, 28 and 37 mm in diameter, and an internal cylinder, simulating the lung. A clinical set of ^{99m}Tc-MAA SPECT and CT images of ten patients, who underwent the radioembolization treatment planning procedure, was selected and retrospectively processed and analyzed. Among these patients, six of them were treated during a single-session of ^{90}Y radioembolization and two had a double-session within the same day. The remaining two patients were excluded from liver radioembolization treatment due to an excessive pulmonary shunt.

Phantom images acquisition was part of the experimental work conducted in the thesis, while clinical images were previously acquired for clinical purposes. The retrospective analysis was completely blind of patient identification. All patients attending the Champalimaud Centre for the Unknown sign informed written consent as per local Ethics Committee guidelines.

2.2 Implementation of SPECT Images Attenuation Correction

Maximum Likelihood Expectation Maximization (MLEM) SPECT images reconstruction was performed through the open source code of the Software NiftyRec 2.0 [10, 11]. For each study, open source software Platform 3D Slicer 4.6 was employed to align CT and SPECT images [12, 13]. A global rigid transformation was applied in order to preserve the anatomical structures, and, as a fine tuning step, CT and SPECT images were also accurately automatically or semi-automatically registered. During image registration, SPECT was considered the reference, while CT the target image.

Attenuation maps at the desired energy of ^{99m}Tc γ-rays were derived from CT images resampled to SPECT image resolution. Specifically, for homoge-

neous and water-based phantoms, linear attenuation coefficients μ were derived from the CT Hounsfield (I_{HU}) units through Equation 1 [14]:

$$\mu = \frac{I_{HU}}{1000} \cdot \mu_{water,E_{140keV}} + \mu_{water,E_{140keV}} \quad (1)$$

where $\mu_{water,E_{140keV}}$ represents the broad-beam linear attenuation coefficient of ^{99m}Tc γ-rays in water. For heterogeneously attenuating human body tissues, the mathematical relationships between I_{HU} units and linear attenuation coefficients of Equation 2 was adopted [14]:

$$\begin{cases} \mu = 0.15 + (1.52 \cdot 10^{-4}) \cdot I_{HU}, & \text{if } I_{HU} < 0 \\ \mu = 0.15 + (1.14 \cdot 10^{-4}) \cdot I_{HU}, & \text{if } I_{HU} > 0 \end{cases} \quad (2)$$

The patient-specific derived attenuation maps were thus incorporated into the process of iterative SPECT image reconstruction, creating attenuation corrected SPECT images. A flowchart summarizing the steps described is here illustrated:

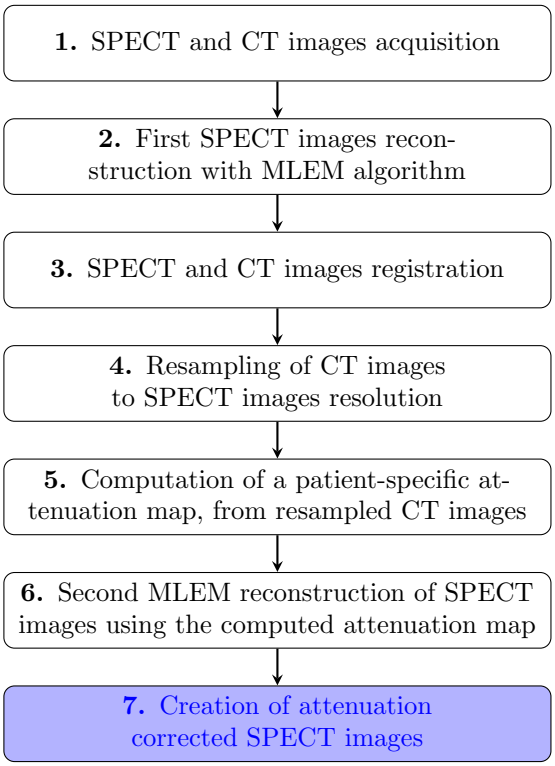

2.3 Appraisal of Attenuation Corrected SPECT Images

Attenuation corrected and uncorrected SPECT phantom and patients' images, obtained with the same reconstruction parameters, were compared using horizontal count density profiles. Image quality was visually evaluated. Furthermore, for NEMA IEC Body Phantom SPECT images, image quality was characterized by several features, such as contrast, Contrast-to-Noise Ratio (CNR) and Signal-to-Noise Ratio (SNR). For this aim, spherical Volumes Of Interest (VOIs), in hot or cold spherical inserts, and within the background area, were identified (Figure 1), as recommended by NEMA [15].

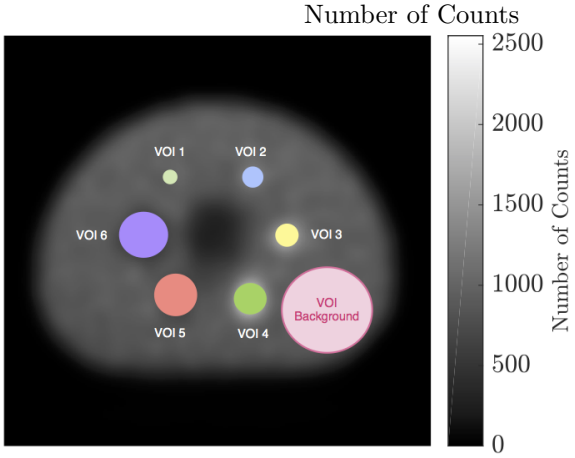

Figure 1 – Illustration of the chosen spheres and background VOIs on NEMA IEC Body Phantom.

In particular, for this aim, the four smallest spherical inserts of the NEMA IEC Body Phantom were filled with an activity concentration 8 times higher than the background activity, while the two biggest ones and the lung insert were left cold, as suggested in scientific literature [15–17]. More specifically, contrast was evaluated for hot and cold spheres by applying Equation 3:

$$Contrast = \left| C_{VOI,Sphere} - C_{VOI,Background} \right| \quad (3)$$

where C represented the mean number of counts in a defined VOI. SNR was calculated for spheres containing ^{99m}Tc following Equation 4:

$$SNR = \frac{C_{VOI,Sphere}}{SD_{VOI,Background}} \quad (4)$$

where SD referred to the standard deviation of the background counts. CNR was derived, for all the spherical inserts, through the Equation 5 [16]:

$$CNR = \left| \frac{C_{VOI,Sphere} - C_{VOI,Background}}{SD_{VOI,Background}} \right| \quad (5)$$

Lastly, according to NEMA standards, to quantify the accuracy of the SPECT imaging attenuation correction method implemented, the relative error, in the lung insert of NEMA IEC Body Phantom, was calculated as follows in Equation 6, by drawing two circular Regions of Interest (ROIs) in the lung insert and in the background, respectively [15]:

$$\Delta Error_{Lung} = \frac{Average\ Counts_{ROI,Lung}}{Average\ Counts_{ROI,Background}} \times 100\% \quad (6)$$

2.4 Activity Quantification in SPECT Imaging

SPECT images measured voxel counts were converted into activity concentration by experimentally determining the actual value of planar sensitivity S of the gamma-camera employed, according to the recommended NEMA standards procedure [15].

The quantitative accuracy of the reconstruction and attenuation correction methodology developed for SPECT imaging was assessed in terms of activity recovery. In this aim, a simpler and costumized configuration of the NEMA IEC Body Phantom was used. The lung insert was filled with a known amount of ^{99m}Tc activity, and SPECT images acquisition was carried out, at first, in air-filled, and then, in water-filled, thorax phantom environment. The recovered activity was determined dividing the total number of recovered counts N during the acquisition time by S, applying Equation 7:

$$Recovered\ Activity\ (\mu Ci) = \frac{N\ (counts/min)}{S\ (counts/min/\mu Ci)} \tag{7}$$

The accuracy was consequently evaluated by the determination of the emission recovery coefficient RC for the customized phantom model both in air and water environment, as in Equation 8:

$$RC = \frac{Recovered\ Activity\ (\mu Ci)}{Decay\ Corrected\ Injected\ Activity\ (\mu Ci)} \tag{8}$$

2.5 Quantitative Agreement between Pre-and-Post-Treatment ^{90}Y Radioembolization Dosimetry

Tumor Volume (TV), Non-Tumor Volume (NTV) and Planning Target Volumes (PTV), for each treated patients, were manually delineated by nuclear medicine physicians on SPECT images, with complementary anatomic information from CT images. Consequently, 3-dimensional S voxel-based dose maps were retrospectively derived from clinical ^{99m}Tc-MAA SPECT pre-treatment images, uncorrected or attenuation corrected, and ^{90}Y PET-CT post-treatment images, through the commercial software STRATOS Dosimetry Solution, a tool of Imalytics Research Workspace of Philips Healthcare (PHILIPS, Amsterdam, The Netherlands).

Intraclass correlation coefficients (ICCs) between predictive and post-treatment dose maps were calculated. The paired Wilcoxon test (significance level 5%) was performed on ICCs values, calculated from both uncorrected or attenuation corrected pre-treatment, and post-treatment dose maps. Moreover, for each PTV and NTV, a predicted-to-actual mean dose ratio ($DR_{PTV,NTV}$) was defined, as reported by Gnesin *et. al.* and indicated in Equation 9 [17]:

$$DR_{PTV,NTV} = \frac{{D_{PTV,NTV,mean}}^{MAA}}{{D_{PTV,NTV,mean}}^{90Y}} \tag{9}$$

Specifically, this ratio permitted to intuitively demonstrate if predictive dosimetry underestimate ($DR < 1$) or overestimate ($DR > 1$) the actual dose delivered to each PTV and NTV.

The commercial software Matlab R2016b was employed for the analysis of the dosimetry data (The MathWorks, Inc., Natick, Massachusetts, United States).

3 Results

3.1 Findings from Phantom Models Studies

Attenuation corrected ^{99m}Tc SPECT images of uniform cylindrical phantom and NEMA IEC Body Phantom were both qualitatively and quantitatively improved as compared to uncorrected ones (Figure 2). Homogeneous activity distribution was observed, and no activity concentration was noticed at the edges of the phantom models (Figure 2b). Greater count density, and contrast between the lung insert and the torso background, were also confirmed (Figure 3).

(a) **(b)**

Figure 2 – Representative axial slice of NEMA IEC Body Phantom SPECT images uncorrected (a) and corrected for attenuation (b). For visualization purposes, the images were normalized by the maximum number of voxel counts.

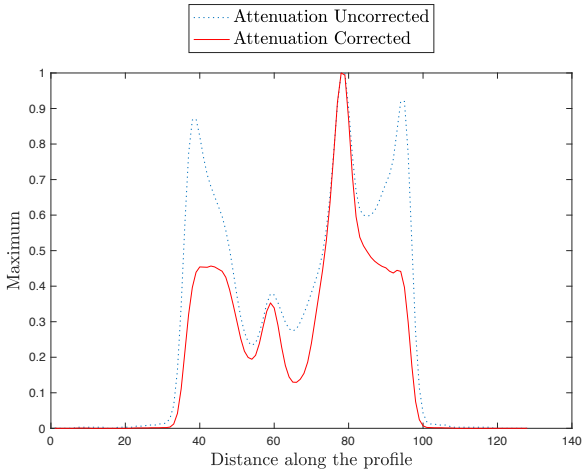

Figure 3 – Uncorrected and attenuation corrected horizontal count density profiles of NEMA IEC Body Phantom images.

Superior image quality of attenuation corrected images was visually apprised. Moreover, higher values of contrast, SNR and CNR were assessed for NEMA IEC Body Phantom (Table 1).

Table 1 – SPECT images quality values of NEMA IEC Body Phantom uncorrected *versus (vs)* corrected for attenuation.

	Contrast	**SNR**	**CNR**
VOI 1	24.5 *vs* 602.5	15.4 *vs* 28.2	1.7 *vs* 5.7
VOI 2	69.7 *vs* 1628	18.5 *vs* 36.7	4.8 *vs* 15.3
VOI 3	83.4 *vs* 3452.7	19.5 *vs* 54.8	5.75 *vs* 32.5
VOI 4	120.8 *vs* 4272.9	22.1 *vs* 62.5	8.3 *vs* 40.2
VOI 5	84.2 *vs* 1019.9	-	5.8 *vs* 9.6
VOI 6	96.9 *vs* 1369.6	-	6.7 *vs* 12.9

The relative error in the lung insert, calculated at three different axial position of the NEMA IEC Body phantom, was found to be, on average, 50% for uncorrected SPECT images, while 25% for corrected ones.

Actual gamma-camera planar sensitivity was approximately 35% inferior than the value indicated by the manufacturer ($\sim$ 177 *vs* 277 $counts/min/\mu Ci$). The total lung insert administered activity was successfully recovered in attenuation corrected SPECT images of NEMA IEC Body Phantom customized models. Specifically, RC percentage values, in air and water background environment, were of 99% and 100%, respectively, and in contrast to 70% and 22% for attenuation uncorrected SPECT images.

3.2 Findings from Clinical Studies

Clinical liver SPECT images, uncorrected for photons attenuation (Figure 4a), did not appear qualitatively different from the corrected ones (Figure 4b).

(a) **(b)**

Figure 4 – Representative coronal slice of liver SPECT images uncorrected (a) and corrected for attenuation (b). For visualization purposes, the images were normalized by the maximum number of voxel counts.

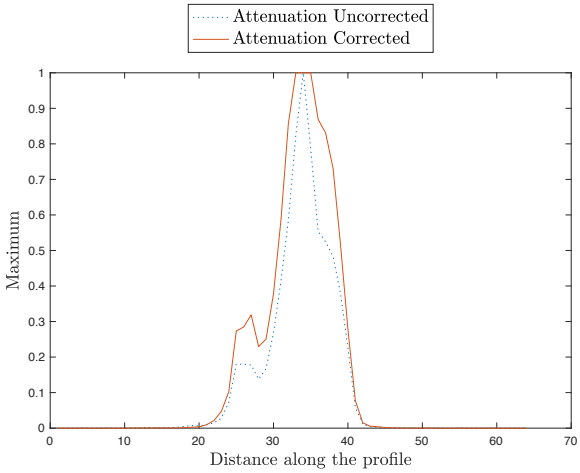

Figure 5 – Uncorrected and attenuation corrected horizontal count density profiles of liver SPECT images coronal slices.

Visual contrast and contour definition were maintained in both images, and no activity concentration at the edges was perceived. However, horizontal count density profiles revealed important quantitative differences, with higher counts density and increased homogeneity of liver ^{99m}Tc-MAA uptake in the attenuation corrected SPECT images as compared to the uncorrected ones (Figure 5).

ICCs between predictive and post-treatment dosimetry maps presented variability, with values as low as 0.023 (Figure 6) and as high as 0.71 (Figure 7) for dose maps derived from attenuation corrected ^{99m}Tc-MAA SPECT images (0.021 and 0.7 for uncorrected SPECT images) (Table 2).

Table 2 – ICCs between uncorrected *vs* attenuation corrected pre-treatment and post-treatment dose maps.

	Uncorrected ICCs *vs* Corrected ICCs
Patient 1	0.54 *vs* 0.54
Patient 2	0.7 *vs* 0.71
Patient 3	0.021 *vs* 0.023
Patient 4	0.14 *vs* 0.41
Patient 5	0.036 *vs* 0.05
Patient 6	0.4 *vs* 0.45
Patient 7	0.11 *vs* 0.12
Patient 8	No treatment
Patient 9	No treatment
Patient 10	0.16 *vs* 0.21

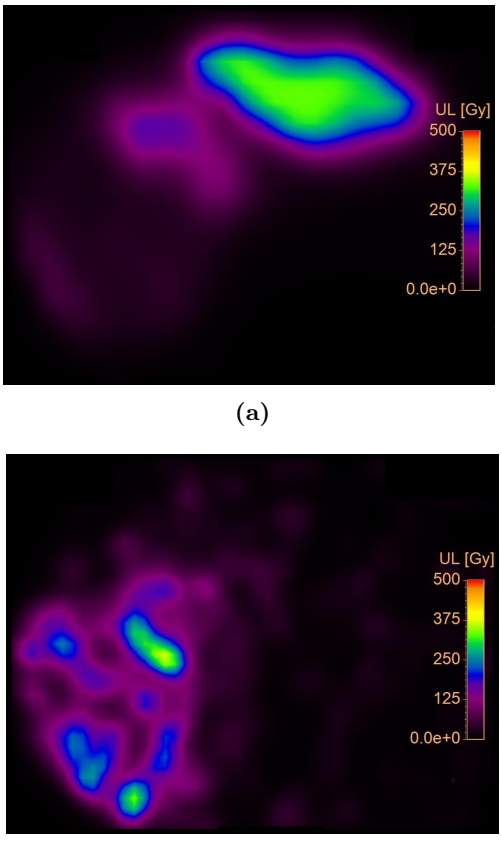

(a)

(b)

Figure 6 – Representative example (same axial slice) of poor correlation between ^{90}Y dose maps of Patient 3, derived from ^{99m}Tc-MAA SPECT images corrected for attenuation (a), and ^{90}Y PET-CT images (b).

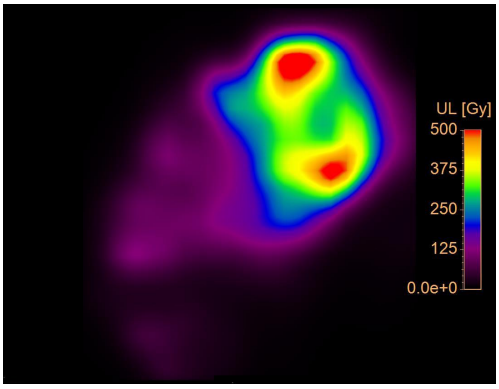

(a)

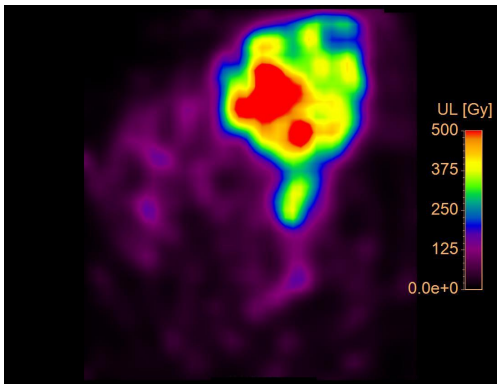

(b)

Figure 7 – Representative example (same axial slice) of high correlation between ^{90}Y dose maps of Patient 2, derived from ^{99m}Tc-MAA SPECT images corrected for attenuation (a), and ^{90}Y PET-CT images (b).

A broad range of DR_{PTV} values was further observed, either if calculated from uncorrected (Figure 8a) or attenuation corrected (Figure 8b) pre-treatment dose maps and ^{90}Y post-treatment ones. Specifically, greater variability was assessed for small tumors than large ones (Figure 9 and Figure 10). DR_{NTV} showed reduced variability as compared to DR_{PTV}, with more frequent values ~ 1 (Figure 8c, 8d).

Paired Wilcoxon test (significance level 5%), performed on ICCs, showed a statistical difference between correlation values derived from uncorrected, or attenuation corrected, ^{99m}Tc-MAA SPECT images *(One-tailed p-value = 0.008)*.

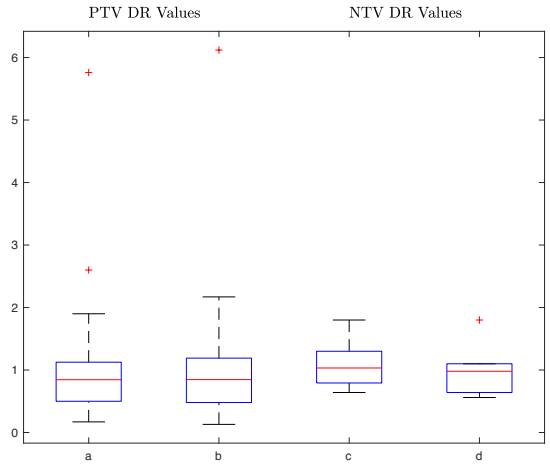

Figure 8 – Boxplot illustrating $\mathrm{DR_{PTV}}$ values computed from uncorrected (a) and attenuation corrected (b) predictive dose maps, and $\mathrm{DR_{NTV}}$ values computed from uncorrected (c) and attenuation corrected (d) predictive dose maps.

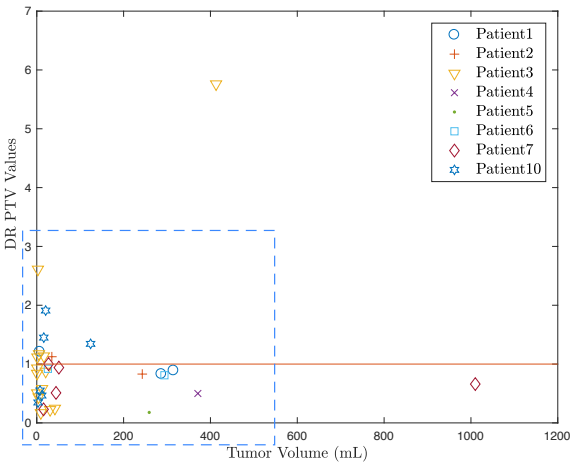

(a)

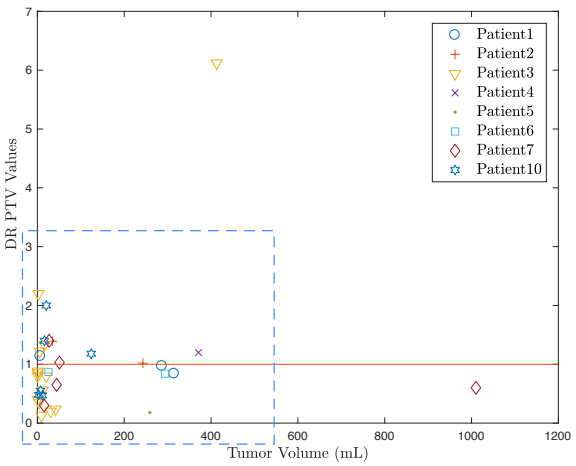

(b)

Figure 9 – $\mathrm{DR_{PTV}}$ values as a function of PTV volume, computed from attenuation uncorrected predictive dose maps (a) and corrected (b).

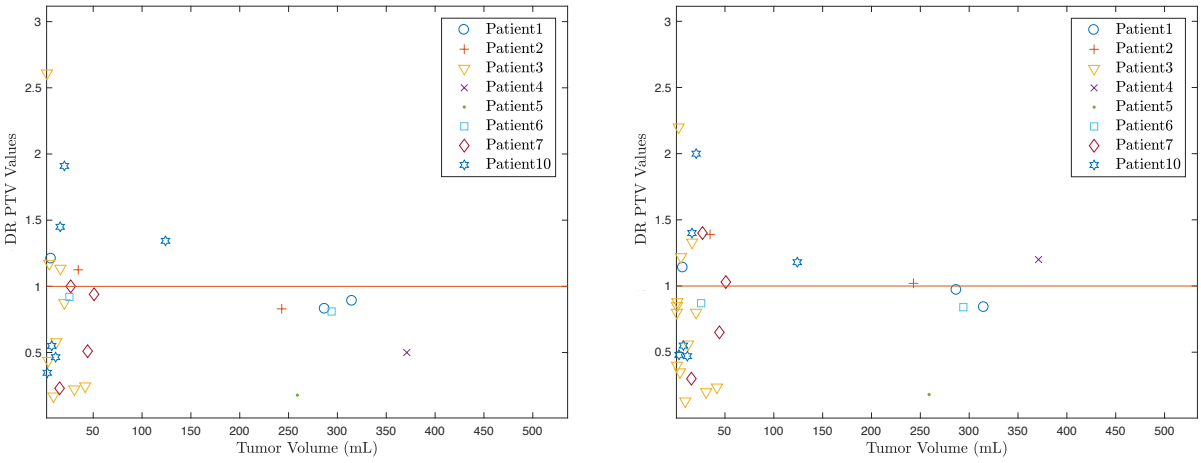

Figure 10 – Zoom of the dashed blue square areas of Figure 9a (a) and Figure 9b (b).

4 Discussion

The studies conducted on phantom models ensured the reliability, of the proposed methodology, to perform quantitative SPECT studies. Namely, CT-based attenuation corrected phantom images were perceptibly improved, and activity quantification was proved to be accurately accomplished in attenuation corrected ^{99m}Tc-based SPECT images.

Results on clinical liver ^{99m}Tc-MAA images confirmed that uncorrected and attenuation corrected images, although qualitatively similar, differed in quantitative aspects. Moreover, the introduction of a patient-specific attenuation correction in pre-treatment ^{99m}Tc-MAA SPECT permitted to increase the quantitative agreement between pre-and-post treatment dosimetry maps. However, frequently, poor and variable correlation were observed, both for dose maps derived from uncorrected, or attenuation corrected, ^{99m}Tc-MAA SPECT images. Thus, this suggested the presence of similarities, as well as inequalities, in the biologic distribution of ^{90}Y-glass microspheres and MAA fragments, as reported in scientific literature [18]. Global disagreement between ^{99m}Tc-MAA and ^{90}Y PET-CT derived dose maps may be explained considering several aspects, such as distinct physical properties of MAA fragments and ^{90}Y microspheres, MAA fragments backflow, differences between SPECT and PET imaging modalities, noisy post-treatment ^{90}Y post-treatment PET-CT images, discrepancies in catheter positioning, for some clinical reason, during pre-treatment SPECT imaging and radioembolization procedure, and ^{99m}Tc-MAA fragments instability, meaning not only in volumetric size, but also in the amount of free pertechnetate, leading to the tecidular diffusion of ^{99m}Tc [19–23]. Moreover, reflux and flow diversion phenomena might occur for small and large tumors, respectively, causing MAA particles distribution to be different from microspheres one [24].

^{99m}Tc-MAA dosimetry showed to well predict the undesired dose delivered to healthy liver tissue. Nevertheless, controversial opinions about its predictive value are present, especially regarding the actual intrahepatic distribution of MAA fragments as compared to ^{90}Y microspheres [21, 22].

The principal limitation of the thesis concerns the limited number of patients involved in the study. For this reason, in future studies, a larger sample should be analyzed in order to obtain firm conclusions.

5 Conclusions

Attenuation correction of SPECT images represents a relevant aspect of *in vivo* activity quantification. Specifically, the quantitative uncertainty related to uncorrected SPECT images may seriously compromise the evaluation of human organs functionality and their abnormalities and, thus, its importance in diagnostic nuclear medicine should be clinically recognized.

In regard to ^{90}Y-labeled glass microspheres liver radioembolization, personalized attenuation correction of ^{99m}Tc-MAA pre-treatment SPECT images permitted to statistically improve its treatment planning. Nevertheless, there is a need to further research in this field. In forthcoming studies, the issues related to the differences between pre-and-post treatment dose maps should be addressed in greater depth. MAA particles are not an ideal model to estimate ^{90}Y-labeled glass microspheres distribution. However, there is a potential predictive power for their use as such, according to the research work underway at the Champalimaud Center for the Unknown, Champalimaud Foundation, Lisbon.

Acknowledgments

I gratefully thank Professors Francisco P. M. Oliveira, Paulo Ferreira, Durval C. Costa, Lidia S. Ferreira and Enrico Maglione for their sincere advice, and guidance, during these months. Moreover, I wish to sincerely acknowledge all the technical staff at the Nuclear Medicine-Radiopharmacology Department, Champalimaud Center for the Unknown, Champalimaud Foundation, Lisbon, and, in particular, Ines Rolo, for their availability, dedication, and without whom all my experiments would have not been possible to be performed.

References

[1] "Cancer Facts & Figures 2016", *Atlanta,GA: American Cancer Society*, 2016.

[2] R. Salem *et al.*, "Yttrium-90 microspheres for the treatment of hepatocellular carcinoma: a review", *Int. J. Radiat. Oncol. Biol. Phys.*, vol. 66, no. 2 Suppl, S83–88, 2006.

[3] M. S. Bhangoo *et al.*, "Radioembolization with Yttrium-90 microspheres for patients with unresectable hepatocellular carcinoma", *J Gastrointest Oncol*, vol. 6, no. 5, pp. 469–478, 2015.

[4] J. C. Camacho *et al.*, "(90)Y Radioembolization: Multimodality Imaging Pattern Approach with Angiographic Correlation for Optimized Target Therapy Delivery", *Radiographics*, vol. 35, no. 5, pp. 1602–1618, 2015.

[5] M. E. Hamami *et al.*, "SPECT/CT with 99mTc-MAA in radioembolization with 90Y microspheres in patients with hepatocellular cancer", *J. Nucl. Med.*, vol. 50, no. 5, pp. 688–692, 2009.

[6] H. Ahmadzadehfar *et al.*, "The significance of 99mTc-MAA SPECT/CT liver perfusion imaging in treatment planning for 90Y-microsphere selective internal radiation treatment", *J. Nucl. Med.*, vol. 51, no. 8, pp. 1206–1212, 2010.

[7] S. A. Gulec *et al.*, "Radiomicrosphere Therapy: Nuclear Medicine Considerations, Guidelines, and Protocols", *J Interv Oncol*, vol. 2, no. 1, pp. 26–39, 2009.

[8] R. Selwyn, "Radiomicrosphere Treatment Dosimetry", *J Interv Oncol*, vol. 2, no. 1, pp. 59–66, 2009.

[9] H. Zaidi *et al.*, "Determination of the attenuation map in emission tomography", *J. Nucl. Med.*, vol. 44, no. 2, pp. 291–315, 2003.

[10] S. Pedemonte *et al.*, "GPU Accelerated Rotation-Based Emission Tomography Reconstruction", *IEEE Nuclear Science Symposuim & Medical Imaging Conference*, 2010.

[11] (), [Online]. Available: `http://niftyrec.sourceforge.net/`.

[12] (), [Online]. Available: `https://www.slicer.org`.

[13] A. Fedorov *et al.*, "3D Slicer as an image computing platform for the Quantitative Imaging Network", *Magn Reson Imaging*, vol. 30, no. 9, pp. 1323–1341, 2012.

[14] S. Brown *et al.*, "Investigation of the relationship between linear attenuation coefficients and CT Hounsfield units using radionuclides for SPECT", *Appl Radiat Isot*, vol. 66, no. 9, pp. 1206–1212, 2008.

[15] "NEMA Standards Publication NU 2-2001, Performance Measurements of Positron Emission Tomographs", *National Electrical Manufacturers Association*, 2001.

[16] S. Oloomi *et al.*, "A New Approach for Scatter Removal and Attenuation Compensation from SPECT/CT Images", *Iran J Basic Med Sci*, vol. 16, no. 11, pp. 1181–1189, 2013.

[17] S. Gnesin *et al.*, "Phantom Validation of Tc-99m Absolute Quantification in a SPECT/CT Commercial Device", *Comput Math Methods Med*, vol. 2016, p. 4 360 371, 2016.

[18] K. Knesaurek *et al.*, "Quantitative comparison of yttrium-90 (90Y)-microspheres and technetium-99m (99mTc)-macroaggregated albumin SPECT images for planning 90Y therapy of liver cancer", *Technol. Cancer Res. Treat.*, vol. 9, no. 3, pp. 253–262, 2010.

[19] P. Haste *et al.*, "Correlation of Technetium-99m Macroaggregated Albumin and Yttrium-90 Glass Microsphere Biodistribution in Hepatocellular Carcinoma: A Retrospective Review of Pretreatment Single Photon Emission CT and Posttreatment Positron Emission Tomography/CT", *J Vasc Interv Radiol*, vol. 28, no. 5, pp. 722–730, 2017.

[20] W. Bult *et al.*, "Microsphere radioembolization of liver malignancies: current developments", *Q J Nucl Med Mol Imaging*, vol. 53, no. 3, pp. 325–335, 2009.

[21] M. Wondergem *et al.*, "99mTc-macroaggregated albumin poorly predicts the intrahepatic distribution of 90Y resin microspheres in hepatic radioembolization", *J. Nucl. Med.*, vol. 54, no. 8, pp. 1294–1301, 2013.

[22] M. L. J. Smits, "Holmium Radioembolization of Liver Metastases", Published thesis, PhD thesis, University of Utrecht, 2013.

[23] S. Gnesin *et al.*, "Partition Model-Based 99mTc-MAA SPECT/CT Predictive Dosimetry Compared with 90Y TOF PET/CT Post-treatment Dosimetry in Radioembolization of Hepatocellular Carcinoma: A Quantitative Agreement Comparison", *J. Nucl. Med.*, vol. 57, no. 11, pp. 1672–1678, 2016.

[24] E. Garin *et al.*, "Clinical impact of (99m)Tc-MAA SPECT/CT-based dosimetry in the radioembolization of liver malignancies with (90)Y-loaded microspheres", *Eur. J. Nucl. Med. Mol. Imaging*, vol. 43, no. 3, pp. 559–575, 2016.